Showcasing research from the Key Laboratory for Ultrafine Materials of the Ministry of Education, East China University of Science & Technology, Shanghai, China.

Litchi-peel-like hierarchical hollow copper-ceria microspheres: aerosol-assisted synthesis and high activity and stability for catalytic CO oxidation

This illustration depicts litchi-peel-like hierarchical copper-ceria microspheres synthesized *via* a facial aerosol route. Highly dispersed CuO_x species and abundant surface steps are obtained in this novel structure. The as-synthesized catalysts exhibit outstanding catalytic activity and stability toward CO oxidation, and can act as strong warriors to eliminate poisonous gas in automotive emissions. Furthermore, the aerosol-assisted technique paves a new way to the fabrication of low-cost and highly efficient environmental catalysts.

As featured in:

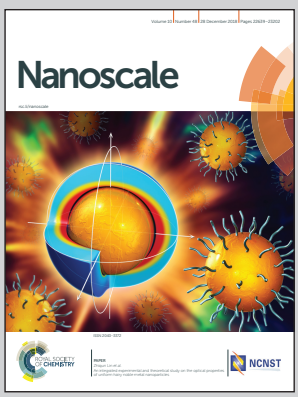

See Yanjie Hu, Chunzhong Li *et al.*, *Nanoscale*, 2018, **10**, 22775.

ROYAL SOCIETY OF CHEMISTRY

rsc.li/nanoscale

Registered charity number: 207890

Nanoscale

PAPER

View Article Online
View Journal | View Issue

Cite this: *Nanoscale*, 2018, **10**, 22775

Litchi-peel-like hierarchical hollow copper-ceria microspheres: aerosol-assisted synthesis and high activity and stability for catalytic CO oxidation†

Wenge Li, Yanjie Hu, * Hao Jiang, Nan Jiang, Wei Bi and Chunzhong Li *

Received 8th June 2018,
Accepted 1st September 2018

DOI: 10.1039/c8nr04642e

rsc.li/nanoscale

Copper-ceria is considered to be a promising system used in exhaust treatment due to its low cost and decent catalytic activity. Herein, we have developed novel litchi-peel-like hollow copper-ceria microspheres with varying Cu contents *via* an aerosol-assisted route. It is found that the dextrin in the spray solution plays a significant role as a sacrificial template and leads to the formation of this hierarchical hollow structure, in which higher surface area and active CuO_x species with higher dispersion result in better catalytic activity compared to the usual hollow samples. The litchi-peel-like sample with 20% Cu exhibits the best reactivity for CO oxidation, namely 50% conversion at 83 °C and 100% conversion at 120 °C. Importantly, this novel copper-ceria sample displays outstanding catalytic stability involving cycle stability, long-term stability and thermal stability, which is attributed to step-stabilized strong interaction between CuO_x species and CeO_2. The superior catalytic activity and stability beyond commercial 5 wt% Pt/Al_2O_3 provides it with the potential to be a substitute for Pt-based catalysts in practical applications.

Introduction

Ceria has gained increasing attention in the field of heterogeneous catalysis such as CO oxidation, soot oxidation, NO reduction and the water–gas shift reaction, due to its unique redox properties and high oxygen storage capacity.[1–6] For CO oxidation, which is an essential functional unit in the treatment of automobile exhaust, a number of ceria-supported noble metal catalysts including Au/CeO_2, Pt/CeO_2 and Pd/CeO_2 have been reported.[7–10] Although desirable catalytic activity has been obtained over them, their high cost and their deactivation when subjected to high temperature hinder their wide application. On the other hand, some transition metal substituted ceria have attracted considerable attention due to their comparable activity to noble metal catalysts and competitive prices.[11–18] In particular, copper-ceria, which has an analogous catalytic activity to cobalt oxides,[19,20] has been considered to be a promising alternative that could substitute noble metal catalysts since it was first reported by Flytzani-Stephanopoulos in 1994.[21] Although CeO_2–Cu_2O with a hollow cage structure and ultrasmall copper doped ceria nanocrystals display enhanced activity and achieve full CO conversion below 200 °C, their catalytic reactivity cannot yet meet the requirement for emission control in current advanced engines.[22,23] Furthermore, owing to the complexity of its intrinsic composition and the various effects of preparation methods and synthesis parameters on catalytic activity, designing a high-performance copper-ceria catalyst is still challenging.

Understanding the nature of active entities and the reaction mechanism can provide a rational strategy for the design of copper-ceria. As revealed in previous studies, the interfaces between finely dispersed CuO_x species and ceria support have been identified as the active sites for CO oxidation, where the strong interfacial interaction induces enhanced oxygen mobility and redox properties *via* the synergetic reaction between Cu^+/Cu^{2+} redox pairs and Ce^{3+}/Ce^{4+} redox pairs.[24–33] Increasing the dispersion degree of active copper species can create abundant interfacial sites and hence improve the catalytic oxidation activity. In addition to the shape effect and the crystal plane effect of ceria,[34–38] which has been extensively explored, the structure and textural properties also have a significant influence on interfacial site population and the corresponding catalytic activity of ceria-supported metal oxides. For instance, Chen *et al.* have fabricated Ce–Mn binary metal oxide hollow nanotubes by an interfacial oxidation–reduction reaction and realized full CO oxidation at 220 °C.[39] In this case, the hollow nanotube structure exposes quantities of interfacial active sites and promotes the catalytic reaction rate. Also, Zhang and co-

Key Laboratory for Ultrafine Materials of the Ministry of Education, School of Materials Science and Engineering, East China University of Science & Technology, Shanghai 200237, China. E-mail: huyanjie@ecust.edu.cn, czli@ecust.edu.cn; Fax: +86-21-64250624, +86-21-64250624; Tel: +86-21-64252055, +86-21-64250949

†Electronic supplementary information (ESI) available. See DOI: 10.1039/c8nr04642e

workers have prepared MnO_2/CeO_2–MnO_2 double shelled hollow spheres, and showed that the synergetic interaction dependent on MnO_2/CeO_2 interfaces contributes to the superior catalytic activity.[40] Therefore, a hollow structure is believed to favor the dispersion of active species and the formation of interfacial sites and has to be extended to the design of a copper-ceria catalyst.

Although many efforts have been devoted to improving catalytic activity, catalytic stability involving cycle stability, long-time stability and thermal stability is also a concern. Since the surface copper species and crystal structure of ceria can be changed during the reaction process and affects catalytic activity, it is necessary to maintain the structural stability of CuO_x/CeO_2 interfaces.[41,42] On the other hand, sintering at high temperature leads to the aggregation of highly dispersed CuO_x clusters and thereby results in the decrease of interfacial sites and the reduction of catalytic performance.[43–45] A typical example is in Curran's report, where the temperature required for full conversion increases from 200 °C to 290 °C as the calcination temperature is ramped from 350 °C to 650 °C.[23] Considering that the temperature of exhaust could be up to 800 °C, remarkable resistance against thermal treatment is required to meet the operating conditions.

In the present work, we have fabricated hollow and novel litchi-peel-like hierarchical hollow copper-ceria microspheres using a facial one-step aerosol spray pyrolysis. Tuning the amount of dextrin used as a sacrificial template in the spray solution results in different hollow structures. High dispersion of copper species and relatively high surface area are obtained in litchi-peel-like hierarchical hollow samples. Interestingly, abundant surface steps are created on the secondary hemispherical hollow shells attached to the main hollow microsphere. In addition, they exhibit better redox properties, as well as superior catalytic activity for CO oxidation, in comparison with the usual hollow samples. Furthermore, the litchi-peel-like sample with 20% Cu content realizes a preferable catalytic activity and stability compared to the commercial 5 wt% Pt/Al_2O_3 catalyst, suggesting its great potential in practical application.

Experimental section

Chemicals

$Cu(NO_3)_2{\cdot}3H_2O$ (99.0%) was purchased from Sinopharm Chemical Reagent Co., Ltd, $Ce(NO_3)_3{\cdot}6H_2O$ (99.5%) and commercial 5 wt% Pt/Al_2O_3 catalyst were purchased from Alfa Aesar, and dextrin was purchased from Shanghai Macklin Biochemical Co., Ltd. All reagents were used without further treatment.

Catalyst preparation

Copper-ceria microspheres were prepared by a facile ultrasonic spray pyrolysis approach. The setup is shown in Fig. S1.† For the synthesis of copper-ceria with varying Cu contents, designed amounts of $Cu(NO_3)_3$ and $Ce(NO_3)_3$ salts and additive dextrin were dissolved in 100 mL deionized water to form the spray solution. The total metal ion concentration was fixed at 0.2 M, and the mass of dextrin was set at 0.2 g and 2 g for the preparation of hollow and litchi-peel-like hierarchically hollow samples, respectively. With the help of an ultrasonic nebulizer with three vibrators (1.7 MHz), numerous droplets were generated from the spray solution and were carried by air flow at a rate of 10 L min^{-1} to obtain a homogeneous aerosol. The quartz tubular reactor was maintained at 800 °C. The aerosol containing precursor droplets were passed through the tubular reactor and then the product was collected on filter paper. The as-synthesized hollow copper-ceria samples with Cu contents (molar ratio of Cu/(Cu + Ce)) of 10%, 20% and 30% were denoted as 10CuCe-H, 20CuCe-H and 30CuCe-H, and the litchi-peel-like hierarchically hollow samples were similarly denoted as 10CuCe-L, 20CuCe-L and 30CuCe-L.

Catalyst characterization

Scanning electron microscopy (SEM) analysis was performed using a Hitachi S-4800 instrument. Transmission electron microscopy (TEM) including bright field scanning transmission electronic microscopy (BF-STEM) and high angle annular dark field scanning transmission electronic microscopy (HAADF-STEM) was performed using a JOEL JEM-2100F instrument equipped with an Oxford energy dispersion X-ray (EDX) detector. The specific surface areas and pore structures were obtained from N_2 adsorption/desorption isotherms at −196 °C recorded using a Micromeritics ASAP 2460 workstation. Surface areas were determined according to the Brunauer–Emmett–Teller (BET) method, and the corresponding pore size distributions were determined from the adsorption branches based on the Barrett–Joyner–Halenda (BJH) method. The crystal structures of samples were investigated by the X-ray diffraction technique. XRD profiles were recorded on a Bruker D8 Advance diffractometer using Cu Kα radiation (λ = 1.5418 Å) at an operating potential of 40 mV and a current of 40 mA. The measurement was carried out in the 2θ range from 10° to 80° with a step size of 0.2°. The crystallite size was calculated by using the Debye–Scherrer formula as shown in eqn (1),

$$D = \frac{0.89\lambda}{\beta \cos\theta} \quad (1)$$

where D is the crystallite size along the given plane, λ is the wavelength of X-ray radiation, β is full width at half maximum of the diffraction peak, and θ is the Bragg angle. Raman spectra were collected using a Horiba Jobin Yvon LabRAM HR microscope equipped with a 532 nm laser. Electron paramagnetic resonance (EPR) analysis was carried out at 25 °C on a Bruker EMX-8/2.7 spectrometer operating at about 9.8 GHz. The microwave power is 2 mW, the modulation frequency is 100 kHz and the modulation amplitude is 0.4 mT. Inductively Coupled Plasma-Atomic Emission Spectrometry (ICP-AES) analysis was carried out using a Perkin-Elmer Optima 5300DV to measure the content of Cu and Ce elements of the as-prepared samples. The X-ray photoelectron spectroscopy (XPS) analysis was performed using a Thermo ESCALAB 250Xi spectrometer

with an Al Kα source (1486.6 eV), and the calibration of binding energies was implemented according to the benchmark of the C 1s peak located at 284.8 eV. Temperature programmed reduction with H_2 (H_2-TPR) analysis was carried out on a chemisorption analysis system (Micromeritics AutoChem II 2920). Prior to the measurement, a 50 mg sample was treated *in situ* in 20% O_2/Ar flow at 300 °C for 0.5 h, and cooled to room temperature. Then it was heated up to 900 °C at a ramp rate of 10 °C min^{-1} in 5% H_2/Ar flow (50 mL min^{-1}).

Catalyst test

The catalytic activity test was carried out by using a continuous-flow fix-bed reactor. Typically, 50 mg catalyst diluted with 200 mg quartz sand (60–100 mesh) was placed between two quartz wool plugs in a quartz tube (I.D. 6 mm). A K-type thermocouple connected to a heating system was embedded in the catalyst bed to control the reaction temperature. Before the measurement, the catalyst was heated in 20% O_2/Ar at 300 °C for 30 min to remove any absorbed residuals and cooled to room temperature. Then a mixed gas consisting of 1% CO, 10% O_2, and balanced Ar was introduced into the tubular reactor with a flow rate of 50 mL min^{-1}, corresponding to a weight hourly space velocity of 60 000 mL h^{-1} g_{cat}^{-1}. The reaction temperature was ramped from 50 to 200 with a step of 10 °C and maintained at each plateau for 30 min to reach a steady state before gas sample analysis. The analysis of outer gas samples was performed on an online gas chromatograph system (GC 2060, Shanghai Ruimin) equipped with a FID detector connected to a methanation oven. The CO conversion was determined according to eqn (2),

$$X_{CO} = \frac{C_{in} - C_{out}}{C_{in}} \times 100\% \quad (2)$$

where X_{CO} is the CO conversion, and C_{in} and C_{out} are the CO concentrations in the inlet gas and outlet gas, respectively.

The catalytic reaction rate measurement was also carried out in the above reactor. 50 mg sample was purged with the mixed gas at a flow rate of 100 mL min^{-1} to make sure that the CO conversion was below 15%. The mass normalized reaction rate in units of μmol s^{-1} g^{-1} was determined using eqn (3),

$$r_{mass} = \frac{X_{CO} \cdot F}{6 \cdot V_m \cdot m_{cat}} \quad (3)$$

where F is the gas flow rate in units of mL min^{-1}, V_m is the ideal gas molar volume in units of L mol^{-1}, and m_{cat} is the mass of the catalyst in units of gram. The area normalized reaction rate was calculated using eqn (4),

$$r_{area} = \frac{r_{mass}}{S_{BET}} \quad (4)$$

where S_{BET} is the surface area of the sample in units of m^2 g^{-1}.

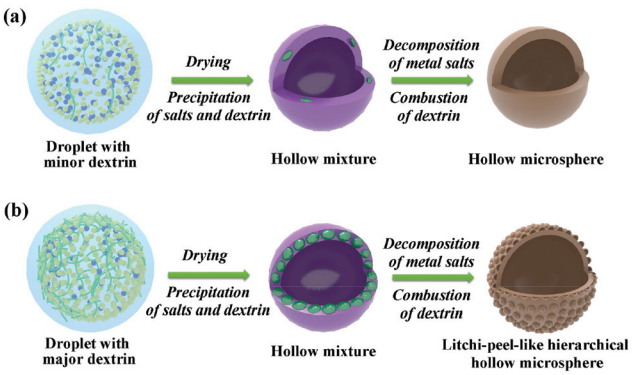

Fig. 1 Schematic formation mechanisms of hollow and litchi-peel-like hierarchical hollow copper-ceria microspheres.

Results and discussion

The schematic formation processes of hollow and litchi-peel-like samples are illustrated in Fig. 1. It can be seen in Fig. 1a that fast drying occurs when the droplet enters the front side of the tubular furnace. At this stage, water evaporates and metal salts and dextrin precipitate on the surface of the droplet to form a hollow spherical mixture. On further heating, the salts begin to decompose into metal oxides, and meanwhile, combustion of dextrin takes place. Afterwards, crystal growth and aggregation under high temperature conditions results in the hollow copper-ceria microsphere. As the mass of the additive dextrin is much less than that of metal salts, its contribution to the pore structure could be neglected. Finally, a usual hollow structure is obtained. As shown in Fig. 1b, the presence of ten times the dextrin amount of the former, however, leads to the formation of quantities of molten dextrin blocks as a result of phase separation in the hollow mixture. Subsequent heating induces the generation of crystallites along the surface of these blocks, but does not cause the combustion of dextrin due to its relatively high thermal decomposition temperature. Thus, a litchi-peel-like hierarchical hollow structure is obtained after sintering. It can be seen that the large amount of dextrin in the spray solution serves as a sacrificial template for the formation of secondary hollow hemispheres.

Fig. 2 depicts the morphologies and structural properties of hollow and litchi-peel-like hierarchical hollow copper-ceria samples. As shown in Fig. 2a, 20CuCe-H displays the usual spherical feature, and has a wide size distribution, which is found to be 0.3–2.0 μm. It can be seen from their enlarged SEM image (Fig. S2†) that the microspheres have a relatively smooth surface. TEM characterization is employed to further investigate the copper dispersion and the structure of the as-prepared copper ceria samples. In the TEM image (Fig. 2b), 20CuCe-H presents a typical hollow microstructure, which has never been seen in previous reports related to spray pyrolysis synthesis. The HAADF-STEM image (Fig. 2c) and the BF-STEM image (Fig. S3a†) evidence a distinct hollow spherical structure with a single shell and the thickness of the shell is found to be

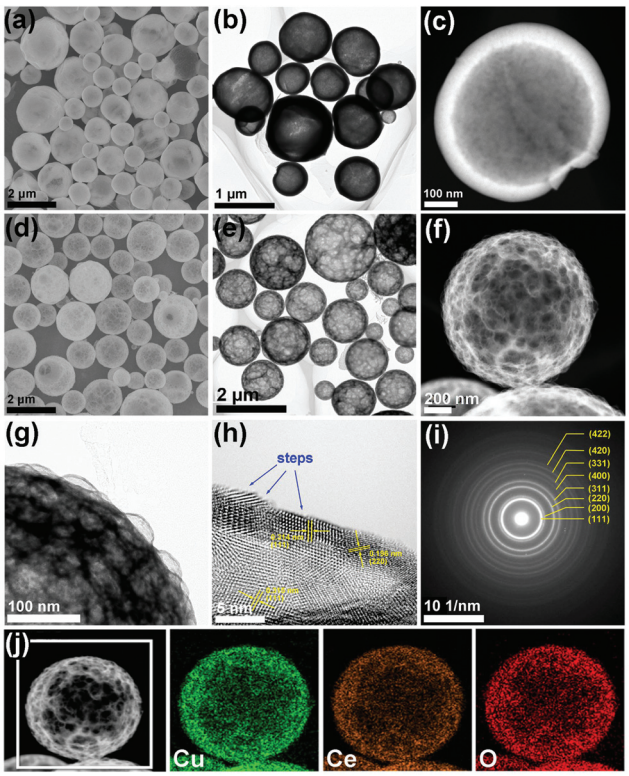

Fig. 2 (a) SEM image, (b) TEM image and (c) HAADF-STEM image of 20CuCe-H, (d) SEM image, (e) TEM image, (f) HAADF-STEM image, (g) magnified TEM image and (h) HRTEM image of 20CuCe-L, (i) SAED pattern of a single microsphere in (f), and (j) elemental EDX mapping of 20CuCe-L.

about 60 nm. It can be clearly seen that the hollow microsphere is constituted by masses of nanocrystallites, which is further confirmed by the enlarged TEM image (Fig. S3b†). Plentiful pores formed by the assembly of nanocrystallites are also observed in the shell.

In the high-resolution TEM (HRTEM) image (Fig. S3c†), the spacings of the selected three lattice fringes are found to be 0.304 nm, 0.268 nm and 0.269 nm, corresponding to the (111) plane, (200) plane and (200) plane of ceria, respectively. It should be noted that no separate CuO or Cu_2O crystal phase can be detected in the HRTEM image, indicating the high dispersion of copper species in the ceria substrate. The selected area electronic diffraction (SAED) image (Fig. S3d†) shows a typical concentric annular pattern, in accord with the behavior of ceria polycrystals. Likewise, the presence of the main characteristic diffraction rings attributed to the (002) plane and (111) plane of CuO or Cu_2O cannot be detected yet. To further investigate the element distribution in the microsphere, an EDX mapping analysis was carried out. As revealed by Fig. S4,† the three elements, Cu, Ce and O, are all homogeneously distributed in the hollow shell, and no aggregation of EDX signals is detected in each mapping graph.

As for the 20CuCe-L sample, it can be seen in Fig. 2d that the microspheres have a more regular spherical shape than the 20CuCe-H sample (Fig. 2a). Obviously, the TEM image (Fig. 2e) displays a hierarchical hollow spherical structure, as well as an average microsphere size of 1.1 μm. The HAADF-STEM (Fig. 2f) and BF-STEM (Fig. S5†) images clearly illustrate the architecture of the unique microsphere. Numerous protuberant semispherical hollow bubbles are found to be supported on the main big hollow spherical shell. Overall, the whole microsphere seems to be a litchi without the sarcocarp. Interestingly, the secondary semispherical protrusion due to the combustion of dextrin is hollow rather than dense, which is different from the particles on the litchi peel. This novel hierarchical hollow structure is further evidenced by the magnified TEM image (Fig. 2g). The thickness of the primary hollow shell is found to be about 10 nm, which is much less than that of 20CuCe-H.

As shown in Fig. 2h, the three distinct crystal fringes are assigned to the (111) plane, (111) plane and (200) plane of cubic ceria, respectively. It should be noted that there is no evidence of a copper-related crystal phase in the ultrathin secondary shell with a thickness of about 4 nm. More importantly, abundant steps can be observed on the surface of the thin shell in the HRTEM image, as well as in Fig. S6.† In order to accommodate the physics construction of hollow semispheres with ultrathin shells, the surface steps are required to form. Furthermore, no trace of any characteristic electronic diffraction patterns associated with copper oxides can be observed in the SAED image (Fig. 2i). The EDX mapping (Fig. 2j) indicates that the copper species is well dispersed within the whole microsphere. To explore the element dispersion in the local region of the litchi-peel-like microsphere, selected-area EDX characterization was also carried out. It can be observed in Fig. S7† that the copper species is highly dispersed in the secondary hollow semispherical shells, as well as in the main spherical shell. The above results demonstrate that the spray pyrolysis technique realize highly dispersed copper species in ceria-based catalysts. Additionally, the effects of Cu content on the morphology and structure of the copper-ceria samples prepared by spray pyrolysis have been investigated. As presented in Fig. 3a and e, 10CuCe-H and 30CuCe-H samples display typical spherical behavior, which is similar to 20CuCe-H. It can be seen from their enlarged SEM images (Fig. 3b and f) that the microspheres have a relatively smooth surface. Notably, some larger particles, which likely

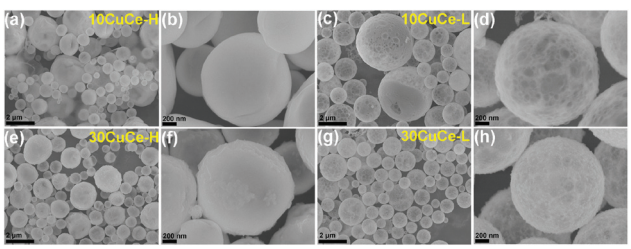

Fig. 3 SEM images of (a, b) 10CuCe-H, (c, d) 10CuCe-L, (e, f) 30CeCe-H and (g, h) 30CuCe-L.

arise from the segregation of excess copper species, are detected on the surface of 30CuCe-H. On the other hand, 10CuCe-L and 30CuCe-L samples (Fig. 3c and g) have similar features to the 20CuCe-L sample.

As for the size of the microspheres, 10CuCe-L possesses a wide range of 0.3–2.5 μm, while 30CuCe-L possesses a relatively narrow distribution of 0.4–1.8 μm. The enlarged SEM images (Fig. 3d and h) show that they have rather different surface morphologies in comparison with the hollow samples. Quantities of protuberant semispherical hollow bubbles are found to be distributed on the surface. It should be noted that the size of hollow bubbles decreases with the increase of Cu content in the sample, suggesting that increasing Cu-containing salt prevents the molten dextrin liquid block from aggregating to form larger blocks. Segregated particles are also observed on the surface of the microsphere in the case of 30% Cu content (Fig. 3f and h). This confirms that the high content is in excess of the doping limit of Cu ions in the ceria lattice.

The structure of hollow and litchi-peel-like samples with varying Cu contents was also studied by TEM characterization. In the case of 10% Cu content, 10CuCe-H (Fig. S8a and b†) displays a hollow structure similar to 20CuCe-H, while 10CuCe-L (Fig. S8c and d†) exhibits a litchi-peel-like hierarchical hollow architecture similar to 20CuCe-L. On account of the lower Cu substitution, it is well understood that the copper species is highly dispersed in the ceria matrix, which is confirmed by their HRTEM images and EDX mapping analysis (Fig. S9, S10 and S11). Importantly, distinct surface steps on the secondary shell can also be observed in the 10CuCe-L sample (Fig. S9b). On the other hand, with the Cu content increasing to 30%, the two samples also present similar morphologies in comparison with those with low Cu content, as shown in Fig. S8e–h.† It should be noted that there are a few large particles on the surface of the microspheres, which can be clearly seen in Fig. S12.† The HRTEM images (Fig. S13†) demonstrate that they are segregated CuO crystals due to the excess doping, in agreement with the observation in SEM images (Fig. 3f and h). Thus, the above results indicate that the Cu content has no significant influence on the structure of copper-ceria microspheres until it exceeds the limit required for the substitution in ceria.

N_2 absorption–desorption experiment was carried out to determine the surface area and pore structure of the copper-ceria samples. As shown in Fig. 4a, the six samples all exhibit a characteristic type IV isotherm, suggesting their mesoporous structure. On the basis of the BET model, the surface areas of 10CuCe-H, 20CuCe-H, 30CuCe-H, 10CuCe-L, 20CuCe-L, and 30CuCe-L were found to be 13.9 $m^2 g^{-1}$, 10.5 $m^2 g^{-1}$, 4.5 $m^2 g^{-1}$, 48.0 $m^2 g^{-1}$, 56.0 $m^2 g^{-1}$ and 58.6 $m^2 g^{-1}$, respectively. The litchi-peel-like hierarchical hollow samples have much larger surface area than the usual hollow samples, which results from the quantities of pores produced by gases generated by the decomposition of enough dextrin in the pyrolysis process. The corresponding pore distributions of the above samples are presented in Fig. 4b. The hollow samples display a narrow distribution of 2 nm to 4 nm, whereas the litchi-peel-like samples display a wide distribution of 2 nm to 90 nm, which is consistent with the results observed in TEM images. The average pore sizes of 10CuCe-L, 20CuCe-L, and 30CuCe-L are found to be 12.2 nm, 12.9 nm and 11.5 nm, respectively. The high surface area and the appropriate pore structure are beneficial for the adsorption of gaseous reactant over the catalysts.

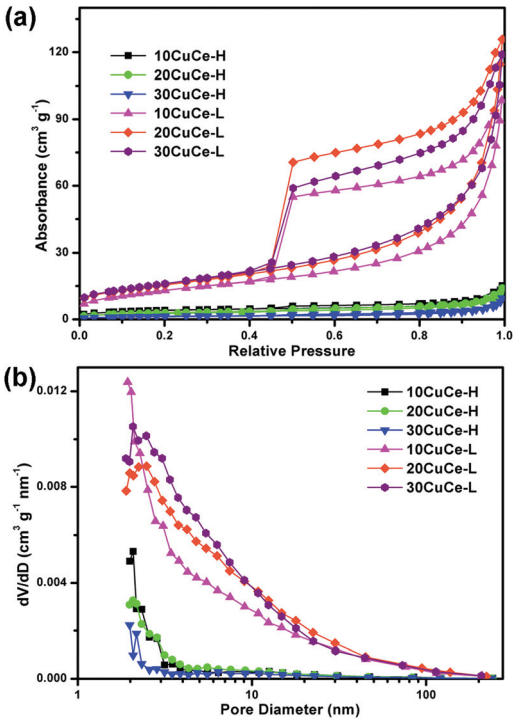

Fig. 4 (a) N_2 adsorption/desorption isotherms and (b) BJH pore distributions of the as-prepared copper-ceria samples.

The XRD patterns of the as-prepared samples with varying Cu contents are presented in Fig. 5. Eight diffraction peaks located at 28.6°, 33.1°, 47.5°, 56.3°, 59.1°, 69.4°, 76.7° and 79.1° can be clearly observed in each sample. They are assigned to the (111), (200), (220), (311), (222), (400), (311) and

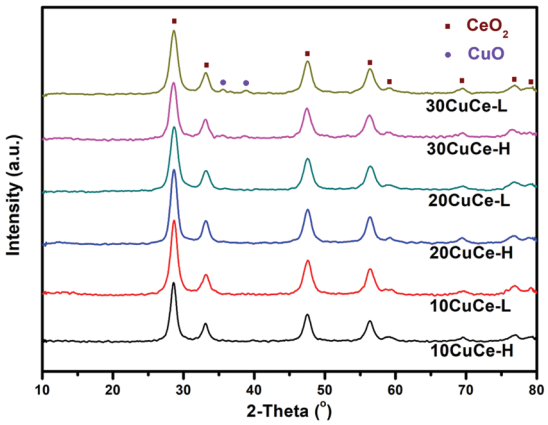

Fig. 5 XRD profiles of the as-prepared copper-ceria samples.

(420) planes of the cubic ceria phase with a fluorite structure (JCPDS No. 34-0394), respectively. There is no evidence of CuO or Cu_2O phases when the Cu content is 10% and 20%, suggesting the existence of copper species during the formation of Cu ions doped in the ceria lattice and finely dispersed CuO_x clusters. While the Cu content increases to 30%, two weak peaks at 35.5° and 38.6° ascribed to the characteristic peaks of CuO (JCPDS No. 48-1548) can be detected. This indicates the presence of bulk CuO crystallites supported on the ceria surface in addition to the highly dispersed Cu species, in the case of a high Cu content.

The broadened diffraction peaks imply that these samples are composed of ultrafine crystallites. According to the Debye–Scherrer equation, the average crystallite sizes of the six samples from the bottom to the top in Fig. 5 are found to be 8.8 nm, 7.3 nm, 7.9 nm, 6.8 nm, 6.6 nm and 5.7 nm, respectively.

It must be noted that each litchi-peel-like sample exhibits smaller crystallite size than the hollow sample with the same Cu content, which is attributed to the inhibition effect of more additive dextrin on the crystal growth in the spray pyrolysis process. Furthermore, the diffraction peaks between 25° and 35° of all copper-ceria samples (Fig. S14†) are found to be slightly shifted to higher diffraction angles compared to the standard ceria, corresponding to the decrease of the lattice parameter. This is due to the incorporation of copper ions in the ceria lattice during the formation of the Cu–O–Ce solution, since the copper ion has a smaller radius than cerium ion.

Raman analysis was undertaken to obtain further information about crystal defects related to oxygen vacancies of ceria-based oxides. As shown in Fig. 6a, all copper-ceria samples exhibit a prominent sharp peak at 450 cm^{-1}, which is considered to be the triply degenerate F_{2g} vibration mode of fluorite structural ceria with the *Fm3m* space group. Clearly, a shift toward low wavenumber of the F_{2g} band compared to pure CeO_2 microspheres can be seen in each sample. This observation indicates the lattice shrinkage attributed to the incorporation of copper ions in the ceria lattice, in good agreement with the results of XRD analysis. Moreover, all copper-ceria samples display a broad so-called defect-induced band D around 600 cm^{-1} due to relaxation of symmetry selection rules as a result of structural perturbations of the ceria cubic lattice, which is not detected in the pure ceria sample. The generation of oxygen vacancies in copper-ceria samples supported by the presence of the band D arises from the Cu substitution in the lattice and self-doping of Ce^{3+} ions. As reported in previous studies, the relative ratio of the area of band D to the area of band F_{2g} can describe the concentration of the oxygen vacancies of copper-ceria materials.[46,47] It can be seen that this ratio over the litchi-peel-like sample is larger than that over the hollow sample with the same Cu content. This demonstrates that the litchi-peel-like hierarchical structure with abundant steps favors the formation of oxygen vacancies.

To obtain further insight into the identification of copper species and oxygen vacancies, X-band EPR spectra analysis was conducted. As seen in Fig. 6b, each copper-ceria sample possesses a sharp peak at g = 2.26, which is confirmed to be attributed to the Cu dimer formed by two equivalent and axially symmetric Cu atoms. With the same Cu content, this peak intensity of litchi-peel-like samples is much larger than that of hollow samples, indicating the presence of more Cu dimers in the former.[48] Notably, the peak intensity increases when the Cu content increases from 10% to 20%, but remains almost the same when it increases from 20% to 30%. This implies that extra Cu species exist in the form of bulked CuO particles, in agreement with the results of TEM and XRD analyses. Moreover, a broad peak at around g = 2.00 can be detected in each sample. This feature peak is ascribed to the adsorbed oxygen radicals associated with oxygen vacancies, according to previous studies.[49] It can be found that the oxygen signal gradually decreases with the increase of Cu content, suggesting that excess copper species could inhibit the generation of oxygen vacancies. Distinctly, litchi-peel-like samples display much stronger oxygen signals compared to hollow samples. This verifies the formation of larger oxygen vacancy population in the novel hierarchical structure, in accordance with the result of Raman spectra analysis.

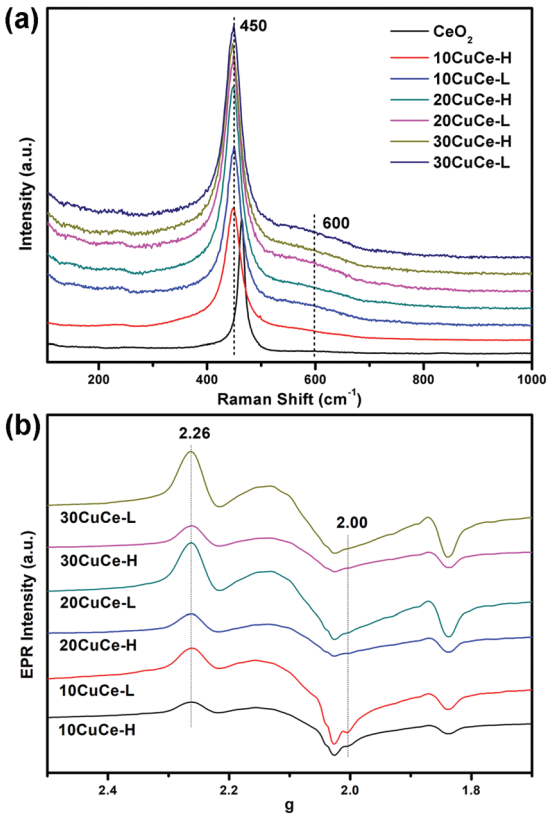

Fig. 6 (a) Raman spectra and (b) EPR spectra of the as-prepared copper-ceria samples.

To investigate the surface components and chemical state of the elements in copper-ceria samples, an XPS experiment was carried out. As shown in Fig. 7a, the characteristic peaks of Cu 2p, Ce 3d and O 1s spin-orbits are observed in all copper-ceria samples. The surface Cu concentration can be

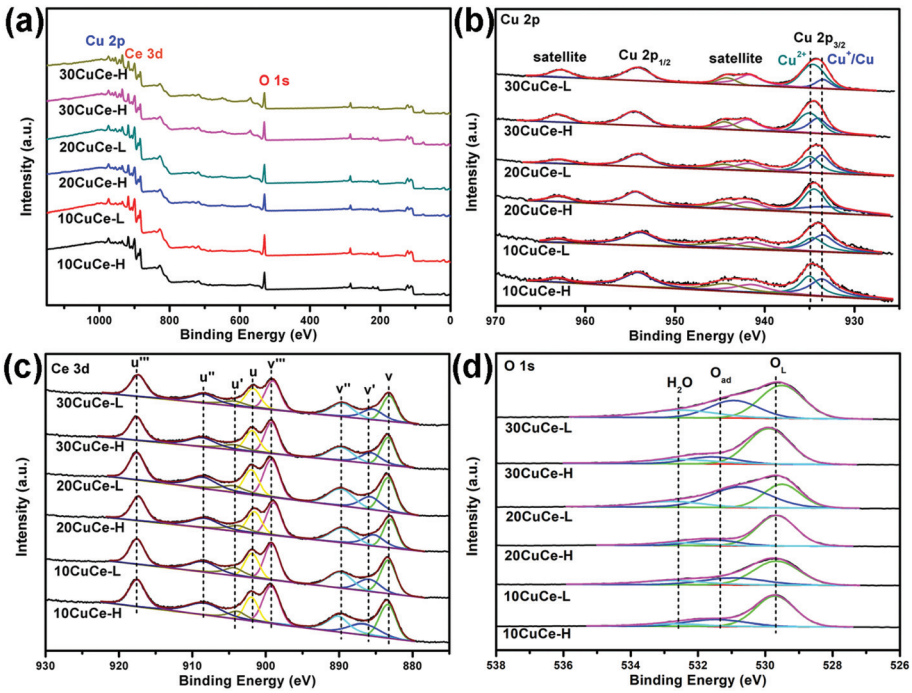

Fig. 7 (a) XPS survey spectra, (b) Cu 2p spectra, (c) Ce 3d spectra and (d) O 1s spectra of the copper-ceria sample.

Table 1 ICP-AES and XPS results for the as-prepared copper-ceria samples

Samples	Cu (wt%)[a]	Cu (wt%)[b]	Cu^+ (%)[c]	Ce^{3+} (%)[d]	O_{ad} (%)[e]
10CuCe-H	3.7	8.9	53.6	15.0	24.2
10CuCe-L	3.7	8.5	57.4	15.8	28.3
20CuCe-H	7.6	13.4	47.9	16.7	18.1
20CuCe-L	7.5	13.0	52.7	16.3	59.3
30CuCe-H	12.4	22.0	47.6	16.5	19.1
30CuCe-L	12.6	25.1	22.1	17.2	37.6

[a] Cu concentration determined by ICP-AES. [b] Cu concentration determined from XPS survey spectra. [c] The ratio of Cu^+ with respect to (Cu^+ + Cu^{2+}) determined from Cu 2p spectra. [d] The ratio of Ce^{3+} with respect to (Ce^{3+} + Ce^{4+}) determined from Ce 3d spectra. [e] The ratio of O_{ad} with respect to (Ce^{3+} + Ce^{4+}) determined from O 1s spectra.

obtained by a comparison of these integrated peak areas in the survey spectrum. The calculated surface Cu concentration and the bulk Cu concentration determined by ICP-AES analysis are listed in Table 1. Clearly, the surface Cu content is approximately twice that in the bulk over all samples. The surface enrichment of copper species, which has been seen in flame-synthesized copper-ceria reported by Kydd *et al.*,[48] indicates that the rapid pyrolysis process leads to the formation of extra copper species on the surface rather than the perfect solid solution and thereby increases the copper coverage.

Fig. 7b presents the Cu 2p spectrum of the above samples. Two main peaks of Cu $2p_{3/2}$ (934.1 eV) and Cu $2p_{1/2}$ (954.0 eV), as well as two shake-up satellite peaks at 943 eV and 963 eV associated with Cu^{2+} ions, are detected in all spectra. The wide Cu $2p_{3/2}$ peak can be fitted to two refined parts, namely the peak at 934.8 eV assigned to Cu^{2+} and the peak at 933.6 eV assigned to Cu^+ or metal Cu. Since the 2p photoelectron peaks of Cu^+ and Cu have the same binding energy, it is difficult to distinguish them. In order to determine the exact oxidation states of copper species, Cu LMM Auger spectroscopy (Fig. S15†) was also carried out. After fitting, the peaks at 568.8 eV and 570.6 eV confirm the presence of Cu^{2+} and Cu^+, and no characteristic peak of metal Cu is detected. Thus, only Cu^+ is responsible for the peak at 933.6 eV in Cu 2p spectra. It can be observed in Table 1 that an increase of Cu content leads to the decrease of the proportion of Cu^+ in both *x*CuCe-H and *x*CuCe-L samples (*x* = 10, 20, 30). Given that the generation of Cu^+ correlates with the reduction of Cu^{2+} by Ce^{3+}, the above effect could be well understood. The stable existence of surface Cu^+ species originates from the strong interaction of CuO_x species and CeO_2 support, which induces a synergetic reaction between Cu^+/Cu^{2+} redox pairs and Ce^{3+}/Ce^{4+} redox pairs.[33,35] For the litchi-peel-like samples, the Cu^+ ratio is found to be larger than that of hollow samples in the case of 10% and 20% Cu content, indicating that the litchi-peel-like hierarchical structure with secondary thin shells enhances the interfacial interaction and leads to the generation of more Cu^+ species.

The Ce 3d spectra of the copper-ceria samples are illustrated in Fig. 7c. As reported in related studies, eight spin–orbit components can be obtained by multiplet splitting. The three pairs of peaks, usually labeled as (u, v), (u′, v′) and (u″, v″), are attributed to the photoelectron spectrum of Ce^{4+}, whereas the pair of peaks, denoted as u and v, are attributed to the characteristic spectrum of the Ce^{3+} species. All samples

are found to have similar proportions of Ce^{3+} ions with regard to the total cerium varying from 15.0% to 17.2%, which is calculated by taking the area ratio of the characteristic peaks of Ce^{3+} species to that of total cerium species.

Fig. 7d shows the O 1s spectra of the copper-ceria samples and three characteristic peaks can be observed for all the samples. The main peak at around 529.7 eV designated as O_L elucidates the existence of lattice oxygen in CuO and CeO_2 phases, the shoulder peak at around 531.3 eV is attributed to the adsorbed oxygen species including O_2^- and O_2^{2-} or oxygen in hydroxyl groups on the surface, and the weak peak at 532.6 eV is ascribed to the adsorbed water. It has been reported that the adsorbed oxygen species serves as active oxygen to react with adsorbed CO, and thus the relative O_{ad} concentration ($O_{ad}/(O_L + O_{ad})$) affects the catalytic oxidation of CO over copper-ceria. The sample with higher O_{ad} proportion is expected to have a better oxygen storage capacity.[50] It is found in Table 1 that the litchi-peel-like hierarchical structure promotes the oxygen absorption and consequently increases the oxygen mobility. Note that *x*CuCe-L samples have higher O_{ad} concentration than *x*CuCe-H samples, which is attributed to the abundant surface steps in litchi-peel-like samples that act as adsorption sites for oxygen. In particular, 20CuCe-L has the highest O_{ad} proportion, implying its promising catalytic oxidation activity.

It is well known that the redox property of copper-ceria correlates with its catalytic reactivity. The H_2-TPR experiment was employed to obtain information about the reducibility and the identification of different copper species. As shown in Fig. 8, two overlapped reduction peaks can be observed below 200 °C for all the samples. According to previous reports, the peak at the lower temperature denoted as α represents the reduction of finely dispersed CuO_x species that have a strong interaction with ceria, while the peak at higher temperature denoted as β is attributed to the reduction of the copper ions in the Cu–O–Ce solid solution.[51,52] Notably, for the samples with 30% Cu content, an additional peak at a higher temperature than β designated as γ is observed. The presence of peak γ results from the reduction of bulk CuO particles on the surface of ceria, which have been confirmed by XRD and TEM analyses. The temperature of each reduction peak for all the samples is listed in comparison with the hollow sample, suggesting the better reducibility of litchi-peel-like samples. Since each reduction peak is responsible for particular copper species, the relative ratio of the area of α associated with highly dispersed CuO_x to the total area can be used to determine the dispersion degree of copper species. Similarly, the ratio (A_α/A_{total}) for litchi-peel-like samples is higher than that of hollow samples with the same Cu content. The higher A_α/A_{total} values indicate that the hierarchical structure with secondary hollow hemispheres facilitates better dispersion of copper species on the ceria surface. In addition to the above three peaks, a weak reduction peak around 750 °C can be detected for all the samples. As unraveled in previous studies, this peak at extremely high temperature refers to the reduction of bulk ceria particles.

The catalytic performance of the as-synthesized copper-ceria was evaluated in a fixed-bed device. As illustrated in Fig. 9a, each litchi-peel-like sample exhibits a better catalytic activity than a hollow sample with the same Cu content. The temperatures required for 50% conversion (denoted as T_{50}) and 100% conversion (T_{100}) are listed in Table 2. The lower conversion temperature of litchi-peel-like samples is attributed

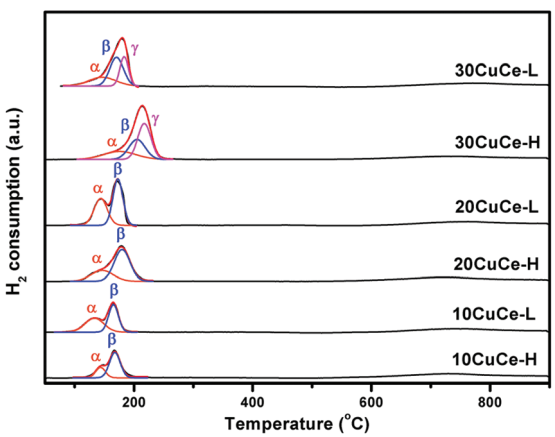

Fig. 8 H_2-TPR profiles of the copper-ceria samples.

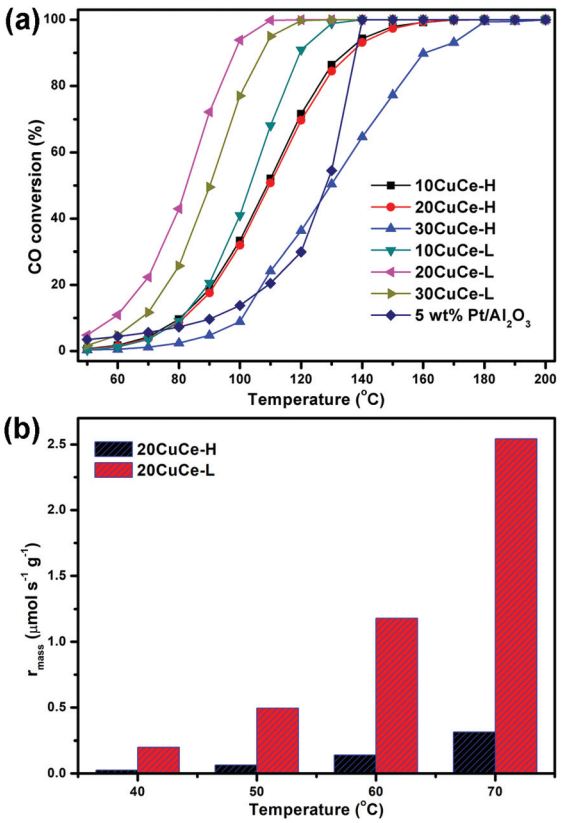

Fig. 9 (a) CO conversion as a function of temperature over the as-synthesized copper-ceria samples, and (b) mass-normalized reaction rates over 20CuCe-H and 20CuCe-L.

Table 2 Redox properties and catalytic activity for the copper-ceria samples

Samples	T_α (°C)	T_β (°C)	T_γ (°C)	A_α/A_{total}	T_{50} (°C)	T_{100} (°C)
10CuCe-H	144	168	—	0.27	109	170
10CuCe-L	134	166	—	0.49	103	140
20CuCe-H	146	179	—	0.32	109	170
20CuCe-L	143	172	—	0.43	83	120
30CuCe-H	177	206	218	0.24	130	180
30CuCe-L	146	170	183	0.27	90	130

to the higher Cu dispersion degree as revealed by TPR analysis as well as the higher surface area, compared to the hollow samples. In particular, 20CuCe-L displays the best activity, namely realizing half CO conversion at 83 °C and full CO conversion at 120 °C. According to Guo's report, a moderate increase of Cu coverage enhances the interfacial interaction.[53] In the case of litchi-peel-like samples, the rise of Cu content from 10% to 20% greatly increases the surface Cu coverage from 8.5% to 13.0% (see Table 1) and there remains a high Cu dispersion with a slight drop from 0.49 to 0.43 in terms of A_α/A_{total} (see Table 2), leading to the overall enhancement of the CuO_x–CeO_2 interaction. However, very high Cu content (30%) causes the significant drop of Cu dispersion and the generation of bulk CuO particles with poor activity, and hence leads to their degradation. As a result, the excellent catalytic activity of 20CuCe-L originates from the combined effects of high Cu coverage and high Cu dispersion. It can't be excluded that the relatively high oxygen vacancy concentration determined by Raman and EPR analyses and the enhanced oxygen storage capacity determined from O 1s spectra also contributed to its high reactivity. This outstanding catalytic activity is superior to those of copper-ceria samples in previous reports under similar reaction conditions, as summarized in Table S1.† Importantly, it is also better than that of the commercial 5 wt% Pt-based catalyst.

It should be noted that increasing the Cu content from 20% to 30% leads to the decrease of catalytic activity, which is ascribed to the drastic decline of Cu dispersion degree (see Table 2), though the surface Cu coverage increases. Previous studies have verified that the strong interaction between CuO_x and CeO_2 can promote CO adsorption and electron transfer between the above two species and facilitate the catalytic reaction cycle including reduction of Cu^{2+} and oxidation of Ce^{3+}.[25,31] Due to the generation of large CuO particles, the interfacial interaction becomes weaker and affects the accomplishment of the synergetic reaction process. This reveals that highly dispersed Cu species can strengthen the CuO_x–CeO_2 interaction and contribute to a significant improvement of catalytic activity in turn.

Compared to the sample with 10% Cu content, the lithic-peel-like sample with 30% Cu content displays an enhanced catalytic activity, while the hollow sample with the same Cu content exhibits a reduced catalytic activity. The activity decrease over hollow samples could be attributed to the shrinkage of the redox property along with the significant drop of the Cu dispersion resulting from the formation of quantities of bulked CuO particles, which is verified by the H_2-TPR analysis. However, the proportion of CuO particles with poor activity in 30CuCe-L is relatively smaller than that in 30CuCe-H, resulting in a slight decrease of reducibility compared to 10CuCe-L as seen in Fig. 8 and Table 2. Therefore, the balance effect between greatly increased copper coverage and slightly decreased redox property gives rise to the activity enhancement over 30CuCe-L. This comparison demonstrates that the litchi-peel-like hierarchical hollow structure could buffer the decrease of the copper dispersion subjected to the increase of the copper content and maintain high catalytic activity.

The catalytic reaction rate measurement was performed to investigate the reactivity at the low temperature. As presented in Fig. 9b, 20CuCe-L shows a much faster mass-normalized rate than 20CuCe-H at each temperature. Additionally, 20CuCe-H displays a relatively high catalytic activity of 0.20 μmol s^{-1} g^{-1} even at 40 °C, which is superior to that of $Cu_{0.1}Ce_{0.9}O_{2-x}$ at a similar temperature (0.1 μmol s^{-1} g^{-1}) in Elias's report.[13] In order to eliminate the influence of surface area, area-normalized reactivity measurements were conducted. It can be seen in Fig. S16† that the area-normalized rate for 20CuCe-L is also larger than that of 20CuCe-H, implying the presence of higher active interfacial site concentration in the litchi-peel-like sample. At 70 °C, a decent rate of 0.045 μmol s^{-1} m^{-2} is achieved over 20CuCe-L, whereas the rate over 20CuCe-H is only 0.029 μmol s^{-1} m^{-2}. This difference is in good agreement with the higher dispersion of copper species in the former.

Fig. 10a illustrates the catalytic cycle stability of 20CeCe-L. As seen in the CO conversion curves, T_{50} increases from 83 °C to 87 °C, and T_{100} stays at 120 °C after three catalytic reaction cycles. In contrast, T_{50} increases from 110 °C to 124 °C and T_{100} also increases from 170 °C to 190 °C for 20CuCe-H (see Fig. S17†). The slight activity decay over 20CuCe-L suggests its decent structural stability.

Additionally, measurements in terms of thermal stability were carried out. As seen in Fig. 10b, T_{100} of 20CuCe-L increases from 120 °C to 140 °C after calcination at 800 °C for 2 h, whereas those of 20CuCe-H and 5 wt% Pt/Al_2O_3 both increase by 40 °C. More importantly, this T_{100} increase over 20CuCe-L is much less than that of copper-ceria catalyst in Sun's and Curran's reports, in which T_{100} of the best sample increases about 100 °C after calcination.[23,54] This further demonstrates the remarkable resistance against thermal treatment of litchi-peel-like samples. It has been proposed that the chemical potential for the Cu dimer at step edges is much lower than that on stoichiometric terrace sites, and is considered to be more stable.[55] So we can attribute the improved thermal stability to the stabilization effect of plentiful surface steps as a kind of crystal defect on the CuO_x/CeO_2 interfacial sites, which is also revealed by Mock *et al.*[56] Thus, step-enhanced strong interaction on interfacial sites maintains the high activity of the copper-ceria sample toward CO oxidation.

Furthermore, in the long-term stability test (Fig. 10c), the CO conversion for 20CuCe-L only decreases from 100.0% to

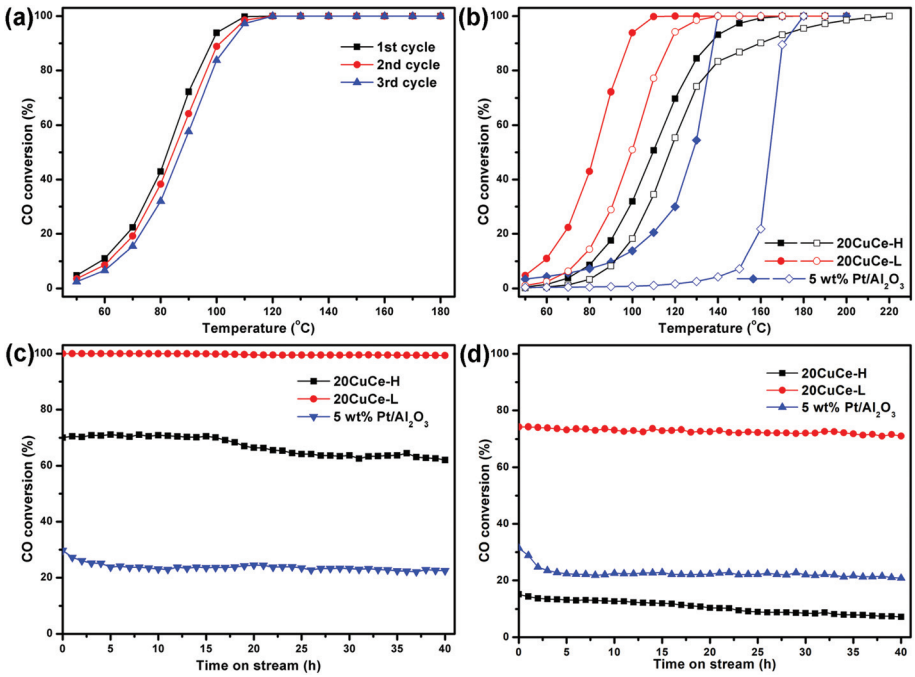

Fig. 10 (a) CO conversion as a function of temperature in three continuous cycles over 20CuCe-L, (b) CO conversion as a function of temperature before (solid) and after (hollow) calcination at 800 °C for 2 h, and CO conversion as a function of time on stream without water (c) and with 5% water (d) at 120 °C over 20CuCe-H, 20CuCe-L and 5 wt% Pt/Al_2O_3.

98.3% after 40 h on the continuous stream at 120 °C. In contrast, a decrease from 70.1% to 61.5% and another from 29.7% to 22.9% are observed for 20CuCe-H and 5 wt% Pt/Al_2O_3, respectively. When 5% H_2O is introduced in the feed gas, both copper-ceria samples display a decrease of catalytic activity, as can be seen in Fig. 10d. After 40 h on stream, the CO conversion drops from 74.2% to 71.1% for 20CuCe-L and from 15.2% to 7.2% for 20CuCe-H. Although the introduction of water somewhat blocks the active sites for CO oxidation, 20CuCe-L still exhibits a much higher CO conversion and a milder shrinkage in comparison with 20CuCe-H and 5 wt% Pt/Al_2O_3 catalysts, indicating its relatively higher resistance against water. Overall, the slight decay over 20CuCe-L indicates that the abundant interfacial active sites remain during long-term catalytic reaction with and without the presence of water, verifying the stability of the litchi-peel-like hierarchical hollow structure.

Conclusions

In this work, a series of copper-ceria with hollow architecture are synthesized by a facial aerosol spray pyrolysis. The copper coverage is tuned by the Cu concentration in the spray solution, while the simple hollow structure and litchi-peel-like hierarchical hollow structure are tailored by the amount of additive dextrin. The production of this novel hollow construction results from the critical role of the sacrificial template dextrin, which induces the formation of secondary hollow hemispheres on the microsphere host. Higher surface area and better Cu dispersion and redox properties are achieved in litchi-peel-like samples in comparison with hollow samples. The optimized litchi-peel-like sample with 20% Cu content shows a low T_{50} of 83 °C and a T_{100} of 120 °C for CO oxidation, which is better than that of 5 wt% commercial Pt/Al_2O_3 catalyst. The outstanding catalytic activity is attributed to the high dispersion of copper species and abundant CuO_x/CeO_2 interface sites. Meanwhile, a remarkable catalytic stability is also realized over this novel copper-ceria sample due to step-promoted stable interfacial active sites. Furthermore, the aerosol-assisted synthesis provides an effective strategy for the rational design of high-performance catalytic systems.

Conflicts of interest

There are no conflicts to declare.

Acknowledgements

This work was supported by the National Natural Science Foundation of China (21522602, 21776092, 91534202, 91534122, 51673063, and 51672082), the Basic Research Program of Shanghai (15JC1401300, 17JC1402300), the Social Development Program of Shanghai (17DZ1200900), Shanghai City Board of Education Research and Innovation Project, and

the Fundamental Research Funds for the Central Universities (222201718002).

Notes and references

1 E. Aneggi, D. Wiater, C. de Leitenburg, J. Llorca and A. Trovarelli, *ACS Catal.*, 2014, **4**, 172–181.
2 Z. Wu, M. Li and S. H. Overbury, *J. Catal.*, 2012, **285**, 61–73.
3 K. A. Michalow-Mauke, Y. Lu, K. Kowalski, T. Graule, M. Nachtegaal, O. Kröcher and D. Ferri, *ACS Catal.*, 2015, **5**, 5657–5672.
4 Y. Cheng, W. Song, J. Liu, H. Zheng, Z. Zhao, C. Xu, Y. Wei and E. J. M. Hensen, *ACS Catal.*, 2017, **7**, 3883–3892.
5 W. Zhan, S. Yang, P. Zhang, Y. Guo, G. Lu, M. F. Chisholm and S. Dai, *Chem. Mater.*, 2017, **29**, 7323–7329.
6 T. R. Reina, S. Ivanova, O. H. Laguna, M. A. Centeno and J. A. Odriozola, *Appl. Catal., B*, 2016, **197**, 62–72.
7 L. W. Guo, P. P. Du, X. P. Fu, C. Ma, J. Zeng, R. Si, Y. Y. Huang, C. J. Jia, Y. W. Zhang and C. H. Yan, *Nat. Commun.*, 2016, **7**, 13481.
8 S. Gatla, D. Aubert, G. Agostini, O. Mathon, S. Pascarelli, T. Lunkenbein, M. G. Willinger and H. Kaper, *ACS Catal.*, 2016, **6**, 6151–6155.
9 J. X. Liu, Y. Su, I. A. W. Filot and E. J. M. Hensen, *J. Am. Chem. Soc.*, 2018, **140**, 4580–4587.
10 A. Lin, A. A. Ibrahim, P. Arab, H. M. El-Kaderi and M. S. El-Shall, *ACS Appl. Mater. Interfaces*, 2017, **9**, 17961–17968.
11 A. J. Binder, T. J. Toops, R. R. Unocic, J. E. Parks 2nd and S. Dai, *Angew. Chem., Int. Ed.*, 2015, **54**, 13263–13267.
12 L. Lukashuk, K. Föttinger, E. Kolar, C. Rameshan, D. Teschner, M. Hävecker, A. Knop-Gericke, N. Yigit, H. Li, E. McDermott, M. Stöger-Pollach and G. Rupprechter, *J. Catal.*, 2016, **344**, 1–15.
13 J. S. Elias, K. A. Stoerzinger, W. T. Hong, M. Risch, L. Giordano, A. N. Mansour and Y. Shao-Horn, *ACS Catal.*, 2017, **7**, 6843–6857.
14 J. W. Qin, J. F. Lu, M. H. Cao and C. W. Hu, *Nanoscale*, 2010, **2**, 2739–2743.
15 W. Liu, X. F. Liu, L. J. Feng, J. X. Guo, A. R. Xie, S. P. Wang, J. C. Zhang and Y. Z. Yang, *Nanoscale*, 2014, **6**, 10693–10700.
16 T. Kou, C. Si, J. Pinto, C. Ma and Z. Zhang, *Nanoscale*, 2017, **9**, 8007–8014.
17 C. Wang, D. Wang, Y. Yang, R. Li, C. Chen and Q. Chen, *Nanoscale*, 2016, **8**, 19761–19768.
18 G. Chen, F. Rosei and D. Ma, *Nanoscale*, 2015, **7**, 5578–5591.
19 H. Yang, K. Lv, J. Zhu, Q. Li, D. Tang, W. Ho, M. Li and S. A. C. Carabineiro, *Appl. Surf. Sci.*, 2017, **401**, 333–340.
20 H. Yang, W. Yang, K. Lv, J. Zhu, Y. Xia, D. Tang and L. Wen, *Microporous Mesoporous Mater.*, 2018, **255**, 36–43.
21 W. Liu, A. F. Sarofim and M. Flytzani-Stephanopoulos, *Chem. Eng. Sci.*, 1994, **49**, 4871–4888.
22 W. Liu, K. Tang, M. Lin, L. T. June, S. Q. Bai, D. J. Young, X. Li, Y. Z. Yang and T. S. Hor, *Nanoscale*, 2016, **8**, 9521–9526.
23 C. D. Curran, L. Lu, C. J. Kiely and S. McIntosh, *J. Mater. Chem. A*, 2018, **6**, 244–255.
24 J.-Y. Luo, M. Meng, Y.-Q. Zha and L.-H. Guo, *J. Phys. Chem. C*, 2008, **112**, 8694–8701.
25 A.-P. Jia, S.-Y. Jiang, J.-Q. Lu and M.-F. Luo, *J. Phys. Chem. C*, 2010, **114**, 21605–21610.
26 D. Gamarra, M. Fernández-García, C. Belver and A. Martínez-Arias, *J. Phys. Chem. C*, 2010, **114**, 18576–18582.
27 K. Wong, Q. Zeng and A. Yu, *Chem. Eng. J.*, 2011, **174**, 408–412.
28 S. H. Zeng, Y. Wang, S. P. Ding, J. Sattler, E. Borodina, L. Zhang, B. M. Weckhuysen and H. Q. Su, *J. Power Sources*, 2014, **256**, 301–311.
29 A. Kubacka, A. Martínez-Arias and M. Fernández-García, *ChemCatChem*, 2015, **7**, 3614–3624.
30 D. Gamarra, C. Belver, M. Fernandez-Garcia and A. Martinez-Arias, *J. Am. Chem. Soc.*, 2007, **129**, 12064–12065.
31 F. Wang, R. Büchel, A. Savitsky, M. Zalibera, D. Widmann, S. E. Pratsinis, W. Lubitz and F. Schüth, *ACS Catal.*, 2016, **6**, 3520–3530.
32 C. S. Polster, H. Nair and C. D. Baertsch, *J. Catal.*, 2009, **266**, 308–319.
33 S. Yao, K. Mudiyanselage, W. Xu, A. C. Johnston-Peck, J. C. Hanson, T. Wu, D. Stacchiola, J. A. Rodriguez, H. Zhao, K. A. Beyer, K. W. Chapman, P. J. Chupas, A. Martínez-Arias, R. Si, T. B. Bolin, W. Liu and S. D. Senanayake, *ACS Catal.*, 2014, **4**, 1650–1661.
34 W.-W. Wang, W.-Z. Yu, P.-P. Du, H. Xu, Z. Jin, R. Si, C. Ma, S. Shi, C.-J. Jia and C.-H. Yan, *ACS Catal.*, 2017, **7**, 1313–1329.
35 M. Lykaki, E. Pachatouridou, S. A. C. Carabineiro, E. Iliopoulou, C. Andriopoulou, N. Kallithrakas-Kontos, S. Boghosian and M. Konsolakis, *Appl. Catal., B*, 2018, **230**, 18–28.
36 M. Zabilskiy, P. Djinović, E. Tchernychova, O. P. Tkachenko, L. M. Kustov and A. Pintar, *ACS Catal.*, 2015, **5**, 5357–5365.
37 S. Zhang, H. Liu, C. Sun, P. Liu, L. Li, Z. Yang, X. Feng, F. Huo and X. Lu, *J. Mater. Chem. A*, 2015, **3**, 5294–5298.
38 Y. Y. Cui and W. L. Dai, *Catal. Sci. Technol.*, 2016, **6**, 7752–7762.
39 G. Chen, F. Rosei and D. Ma, *Adv. Funct. Mater.*, 2012, **22**, 3914–3920.
40 J. Zhang, Y. Cao, C. A. Wang and R. Ran, *ACS Appl. Mater. Interfaces*, 2016, **8**, 8670–8677.
41 C. Yang, X. Yu, S. Heissler, A. Nefedov, S. Colussi, J. Llorca, A. Trovarelli, Y. Wang and C. Woll, *Angew. Chem., Int. Ed.*, 2017, **56**, 375–379.
42 P.-P. Du, W.-W. Wang, C.-J. Jia, Q.-S. Song, Y.-Y. Huang and R. Si, *Appl. Catal., B*, 2016, **518**, 87–101.

43 A. L. Camara, A. Kubacka, Z. Schay, Z. Koppany and A. Martinez-Arias, *J. Power Sources*, 2011, **196**, 4364–4369.
44 G. Aguila, S. Guerrero and P. Araya, *Appl. Catal., A*, 2013, **462**, 56–63.
45 Z.-G. Liu, S.-H. Chai, A. Binder, Y.-Y. Li, L.-T. Ji and S. Dai, *Appl. Catal., A*, 2013, **451**, 282–288.
46 Y. Li, Z. Wei, F. Gao, L. Kovarik, R. A. L. Baylon, C. H. F. Peden and Y. Wang, *ACS Catal.*, 2015, **5**, 3006–3012.
47 S. Putla, M. H. Amin, B. M. Reddy, A. Nafady, K. A. Al Farhan and S. K. Bhargava, *ACS Appl. Mater. Interfaces*, 2015, **7**, 16525–16535.
48 R. Kydd, W. Y. Teoh, K. Wong, Y. Wang, J. Scott, Q.-H. Zeng, A.-B. Yu, J. Zou and R. Amal, *Adv. Funct. Mater.*, 2009, **19**, 369–377.
49 A. Martínez-Arias, M. Fernández-García, J. Soria and J. C. Conesa, *J. Catal.*, 1999, **182**, 367–377.
50 A. B. Dongil, B. Bachiller-Baeza, E. Castillejos, N. Escalona, A. Guerrero-Ruiz and I. Rodriguez-Ramos, *Catal. Sci. Technol.*, 2016, **6**, 6118–6127.
51 M. F. Luo, Y. P. Song, J. Q. Lu, X. Y. Wang and Z. Y. Pu, *J. Phys. Chem. C*, 2007, **111**, 12686–12692.
52 W.-W. Wang, P.-P. Du, S.-H. Zou, H.-Y. He, R.-X. Wang, Z. Jin, S. Shi, Y.-Y. Huang, R. Si, Q.-S. Song, C.-J. Jia and C.-H. Yan, *ACS Catal.*, 2015, **5**, 2088–2099.
53 X. L. Guo, J. X. Mao and R. X. Zhou, *J. Power Sources*, 2017, **371**, 119–128.
54 S. S. Sun, D. S. Mao, J. Yu, Z. Q. Yang, G. Z. Lu and Z. Ma, *Catal. Sci. Technol.*, 2015, **5**, 3166–3181.
55 T. E. James, S. L. Hemmingson and C. T. Campbell, *ACS Catal.*, 2015, **5**, 5673–5678.
56 S. A. Mock, E. T. Zell, S. T. Hossain and R. G. Wang, *ChemCatChem*, 2018, **10**, 311–319.